Individual process development of single and multi-material laser melting in novel modular laser powder bed fusion system

Schanz, Jochen; Islam, Nabirul; Kolb, David; Harrison, David K.; De Silva, Anjali K.M.; Goll, Dagmar; Schneider, Gerhard; Riegel, Harald

Published in:
Progress in Additive Manufacturing

DOI:
10.1007/s40964-022-00276-9

Publication date:
2022

Document Version
Publisher's PDF, also known as Version of record

Progress in Additive Manufacturing (2022) 7:481–493
https://doi.org/10.1007/s40964-022-00276-9

FULL RESEARCH ARTICLE

Individual process development of single and multi-material laser melting in novel modular laser powder bed fusion system

Jochen Schanz[1,2,3] · Nabirul Islam[1] · David Kolb[1] · David K. Harrison[2] · Anjali K. M. De Silva[2] · Dagmar Goll[3] · Gerhard Schneider[3] · Harald Riegel[1]

Received: 22 August 2021 / Accepted: 2 February 2022 / Published online: 7 April 2022

Abstract
Additive manufacturing and especially the laser-based powder bed fusion (LPBF) with full melting of the powder offers tremendous potential and versatility for manufacturing high quality, complex, precision metal parts. However, for novel powder compositions the LPBF process development is very time consuming and cost intensive due to the layer wise melting and the powder prices. This research work investigates the manufacturing of single and layered multi-material structures in a novel modular lab-scaled LPBF machining system through individual process and material development. The developed system allows the use of different laser sources, optical arrangements, individual sensor and actuator integration. In addition, the modular LPBF system enables the manufacturing of specimens with a minimum amount of powder, individual mixed powder compositions or layered multi-material parts. In an application example, a multi-material specimen made out of stainless steel 316L and Bronze 90/10 was manufactured in alternating layers. For this approach, a parameter study was performed for each material to investigate the influence of the volumetric energy density (VED) on the specimen density, surface flatness and reduced mixing zone formation. Afterwards, optimized parameters were used to demonstrate the feasibility of the system to produce a multi-material layered 316L-Bronze part.

Keywords Additive manufacturing · Selective laser melting · Multi-material · Layered structure · 316L stainless steel · 90/10 Bronze

1 Introduction

Laser powder bed fusion (LPBF), also known as selective laser melting (SLM), with a full melting of powder, belongs to the most widely used Additive Manufacturing (AM) processes for building complex 3D metal parts with high level of detail [1]. The advantages of LPBF are the great freedom of design, relative low material waste compared to subtractive manufacturing e.g. milling or turning, time efficiency and the specific adaptability of component and material properties [2]. In principle, all meltable and weldable materials can be processed [3]. In addition, LPBF makes it possible to manufacture parts made of different material combinations as well as geometries and functionalities that are not possible by conventional manufacturing processes [4]. In recent times, a large number of investigations have been carried out for multi-material components with different system concepts [5, 6]. Thereby, the function and performance of AM components can be significantly increased through the specific integration of several different chemical and physical materials in one component (multi-material component). Possible applications for multi-material components are soft magnets with a layered structure, components with layers of particularly conductive materials (heat exchangers) or the increase of the component strength at points subject to higher loads without having to compromise on lightweight construction. These could be used in aerospace, electronics, sensor technology and medical technology, among others.

As all laser-based processes have complex physical, chemical and materials interactions, the material

✉ Jochen Schanz
Jochen.Schanz@hs-aalen.de

[1] Laser Application Center, Aalen University, Beethovenstr. 1, 73430 Aalen, Germany

[2] School of Computing, Engineering and Built Environment, Glasgow Caledonian University, Cowcaddens Rd, Glasgow G4 0BA, UK

[3] Materials Research Institute Aalen, Aalen University, Beethovenstr. 1, 73430 Aalen, Germany

characteristics and process parameters greatly influence the microstructural and mechanical properties of LPBF parts [7–10]. Table 1 summarizes the important process parameters of LPBF.

Due to the multitude of process parameters involved, industrial LPBF machines are not very suitable for R&D needs when investigating novel material compositions. Generally, the industrial machines are designed for specific materials, e.g. stainless steel, and limited in process parameters adjustments. Both, the laser source and the optical components are fixed and the LPBF machines have relatively large building chambers to contain the greater powder volumes required for industrial production. Furthermore, industrial LPBF machines have only one powder reservoir, hindering the development of multi-material components. In addition, most LPBF machines also do not allow the processing of materials with highly oxidation-sensitive contents i.e. neodymium for hard magnets [12] or the simple installation of additional sensors and actuators for process monitoring.

Due to these numerous disadvantages of industrial LPBF machines and the required flexibility for R&D, several research groups have started to develop different types of LBPF systems for novel applications and material research. Wei et al. developed a system to manufacture layered and 3D printed functionally graded specimens with a recoater and several powder dispenser systems. The system allows manufacturing components with autonomous selection of several materials [13]. Researchers from the University of Manchester have demonstrated manufacturing multilayer and functionally graded components using ultrasonic dispenser nozzles to deposit powder locally [14] or by a system with an integrated powder mixer [15–17]. But these processes are time consuming and require sophisticated integration to ensure the process accuracy. Stichel et al. have introduced an electrographic powder deposition process for AM which seems to be a promising technique for multi-material deposition [18, 19]. However, this technique is still under development process. Furthermore, Demir et al. demonstrated a double powder feeder system for the LPBF process. The system is composed of two upper hoppers housing the powder materials and a lower mixing hopper. The hoppers can be operated separately for single material processing or for mixing two different materials together [20]. Chivel introduced a concept of a SLM machine for multi-material parts production where a recoating system with a roller or a blade can be used. The main idea includes a building platform with a cleaning system to separate the various material powders for reuse [21]. So far, Regenfuß et al. developed a vacuum chamber to deposit two different materials independently to fabricate micro multi-material parts by laser sintering [22].

When building up layers of different materials, the evenness of the built-up layers is of particular importance to apply a consistently thick powder layer and to minimize the mixing zones between the two materials [23]. Depending on the material composition, material mixtures lead to undesirable, particularly brittle material compositions, which may result in cracks. Furthermore, the mechanical and physical properties of the built specimens change. One method is the optimization of the parameters of the LPBF melting process, to generate even layers. The volumetric energy density (VED) effect the density, roughness and evenness [24, 25]. It has been shown that a higher VED improves the wetting of the molten material on the surface and increases the flowability, which fills defects [26]. Gu et al. showed that a larger melt pool has a surface smoothing effect due to an increased energy input [27]. However, Wang et al. showed that an excessive VED leads to a higher surface roughness and to an increase of the specimen porosity [24]. In another work it was found that the laser power, the feed rate and the combination of both have a significant influence on porosity and cracking [28]. Another method of reducing the roughness of the individual layers is based on remelting the surfaces of the previously built-up layer before a new layer of powder is applied [29, 30].

One aspect that also needs to be addressed when using different powder materials within a process is powder recycling. Basically, three methods are possible: (I) by size (sieving), (II) density (sedimentation) and (III) magnetic difference [31, 32].

In this research work, a modular LPBF system is developed and demonstrated which gives the flexibility to be adapted to different materials, laser sources and laser processing optics. Since the production of novel material compositions is time and cost consuming, the concept allows

Table 1 Important LPBF process parameters according to [11]

LPBF process parameters			
Laser-related	Scan head-related	Powder-related	Temperature-related
Wavelength	Scanning speed	Particle size and distribution	Powder bed temperature
Laser power	Scanning spacing	Particle shape	Temperature uniformity
Pulse duration	Scanning pattern	Powder bed density	Powder feed temperature
Spot size		Layer thickness	
Pulse frequency		Material properties	
		Powder bed homogeneity	

flexible selection of multiple powder types in one machining process to produce layered multi-material parts. To demonstrate the flexibility of the developed modular LPBF system, two materials with different properties and visual appearance, stainless steel 316L and Bronze 90/10, were selected to fabricate. At initial stage, 316L and Bronze specimens were fabricated separately. Later, optimized sets of parameter for each material regarding to surface flatness and specimen density were chosen to manufacture a layered multi-material structure of 316L and Bronze to demonstrate the usability and possibility of the developed modular LPBF system.

2 Key features of the LPBF concept

Laser beam sources and processing optics are the fundamental components for a precision laser melting process. The conversion of industrial LPBF machines especially to other laser wavelengths or optical setups is complicated and costly. To solve this, a modular LPBF system has been designed (dimensions of 240 mm × 200 mm × 300 mm) for high mobility to use it in different laser cells with various laser sources and processing optics. It is also possible to monitor the quality and volume of different gases. The system allows the use of different sensors and actuators for process monitoring and controlling. The comparable big process window enables a monitoring of the LPBF process with thermography and high speed cameras. The developed LPBF system can be easily operated with up to four different powder types within one build job. The accessibility to the powder reservoirs allows quick refilling or replacement of material within 3 min without residual of the replaced powders. The coating time of a new powder layer is approximately 5 s. Regarding thermal effects, a waiting time between the exposures of two layers can be set. Also, the laser setup change is possible within a short time. The concept is usable for material and process development based on small amount of powders, the rotating powder reservoirs is powder-saving. For instance, in this study, 16 cubes consisting of 316L with the size of 5 mm × 5 mm and a build height of 0.5 mm lead to a volume of 200 mm^3. The substrate plate has a diameter of 40 mm. With a build height of 0.5 mm, a volume of approx. 628 mm^3 of powder is necessary to fill up the complete build chamber with powder. For the balancing of the difference between the density of the powder (4.4 g/cm^3) and the built part (7.98 g/cm^3) bulk density, the volume of approx. 163 mm^3 is added to the 628 mm^3 which lead to an overall necessary powder volume of 791 mm^3 to conduct the parameter study. In Fig. 1, an overview of the modular LBPF concept and its main features are given.

3 Experimental setup and evaluation methods

To demonstrate the capabilities of the modular LBPF concept, two different powder materials, a stainless steel TRUMPF 316L-A LMF (called 316L) and a Bronze alloy TRUMPF Bronze 90/10-A LMF (called Bronze) were used. Table 2 contains information about the powder materials used.

These materials were chosen due to the distinct differences in their mechanical and physical properties. The laser parameter study was carried out in a laser robot cell using a TRUMPF TruFiber 1000 fiber laser with a maximum laser output power of 1000 W in near-infrared wavelength (1075 nm ± 7 nm) and a 2D scan head intelli*SCAN* 30 from SCANLAB, which was mounted on a KUKA KR30 HA robot. The focused laser beam had a diameter of 46 µm. The material of the building platform was carbon steel 1.0503 (C45). The parameter studies as well as the layered built-up were carried out on the C45 substrate material, since in an alternating layered structure the stainless steel 316L with its thermal conductivity of approx. 14.3 W/(m·K) [33], which is only about one third of the Bronze (approx. 43.6 W/(m·K) [34]), always results as a barrier for the heat flow in the layered component. Therefore, no parameter studies were carried out on a Bronze substrate. Prior and during the LPBF processing, the process chamber was flooded with shielding gas, argon (ultra high purity 5.0 grade), at a flow rate of 20 l/min. The gas was initiated with a cross jet, which is mounted directly under the chamber window. Figure 2 shows the complete experimental setup.

To achieve an alternating layered multi-material part of two different materials, expedient laser process parameters of each material were developed. The 316L and the Bronze specimens were fabricated individually in the process chamber to observe influences of the process parameter on these two dissimilar materials. For this approach, a powder layer thickness t of 50 µm and a laser beam hatch distance h of 46 µm (corresponds to the focused laser beam diameter) was defined. The laser power P and the velocity of the laser beam v was variated in a 4 × 4 matrix. The footprint of each specimen was 5 mm × 5 mm. For both materials, the hatch strategy was kept constant in one direction and the relative hatch angle of each layer was remained unchanged (0°). For 316L, the laser power was variated within 150 W and 300 W and the laser beam velocity between 300 and 600 mm/s. For Bronze, the ranges were variated within 120 W and 270 W and between 500 and 800 mm/s in four steps, respectively. After the pre-investigations, suitable parameter combinations for each material were used to build-up an alternating layered multi-material structure consisting of both materials. The specimen's surfaces of the pre-investigations and

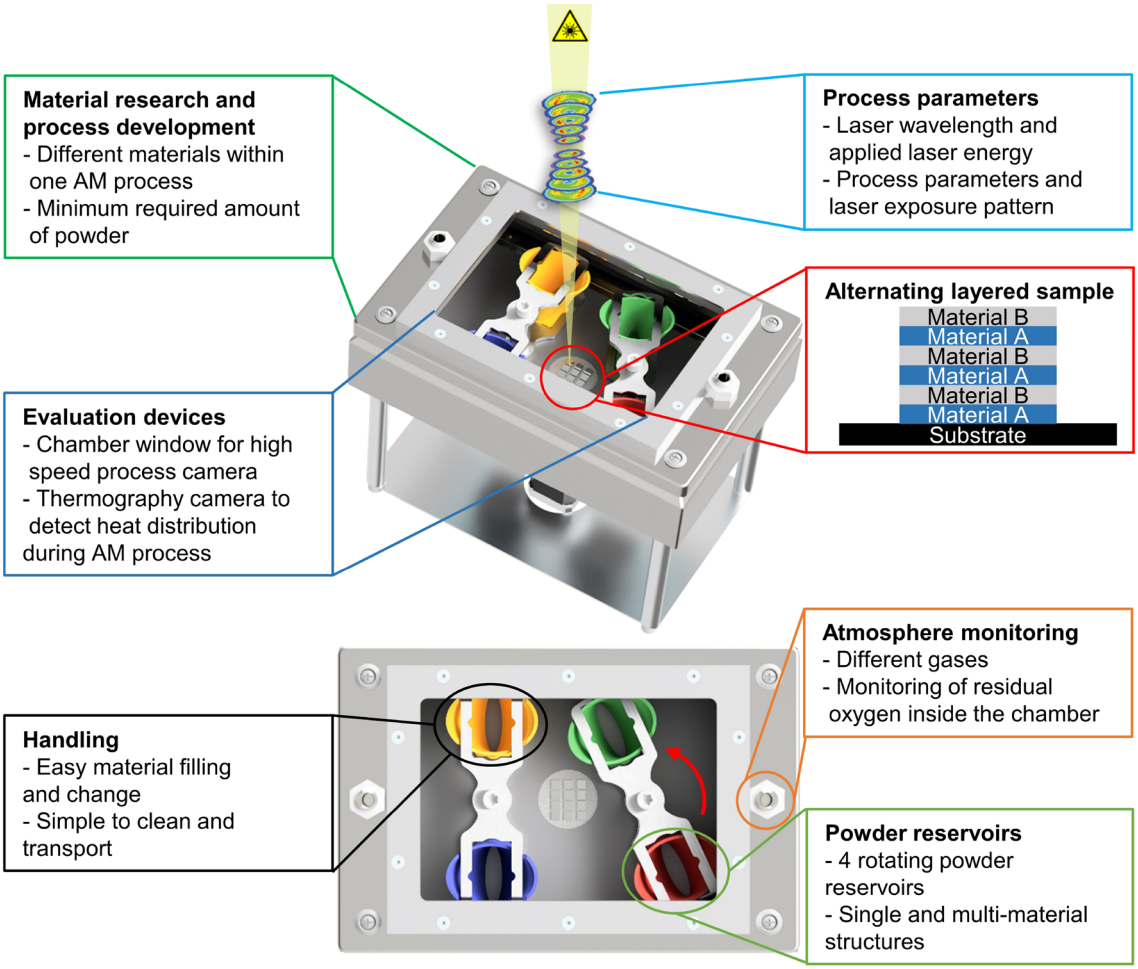

Fig. 1 Overview of the modular LBPF concept and its main features

the layered multi-material specimen were optically analyzed using an Axio Zoom.V16 optical microscope from Carl Zeiss. The topography of the 316L and the Bronze specimens were measured by a KEYENCE VR–3100 profilometer. Afterwards, cross sections of the specimens were made to investigate the single and the layered multi-material specimen microstructures with a Carl Zeiss Axio Imager.Z2 Vario optical microscope.

In this research work, the fabricated specimens are analyzed and discussed according to their corresponding volumetric energy density (VED). Here, VED is the ratio between the laser power P and the product of the laser beam velocity v, the laser beam hatch distance h and the powder layer thickness t (Eq. 1) [11].

$$\mathrm{VED} = \frac{P}{v \times h \times t}. \tag{1}$$

Both for 316L and Bronze, four specimens each are shown to illustrate the influence of the volumetric energy density on the surface homogeneity and specimen density. Among the four selected specimens, the first specimen is fabricated at minimum VED, the second and third specimens are built at higher VED. The forth specimen is fabricated at maximum VED.

4 Results and discussion

4.1 Parameter study with 316L

In a first step, suitable parameters which enable a dense specimen, the flatness of the surface and minimized mixing zone to the underlying layer are searched. The parameters laser power and laser beam velocity significant effect the specimen density and crack formation [28] as well as the surface homogeneity and flatness. In Fig. 3, the surfaces of the final manufactured 316L specimens after ten layers are given.

In Figs. 4, 5, the surfaces of the four selected 316L specimens S1–S4, marked in Fig. 3, are given in more detail.

Table 2 Information about the used TRUMPF 316L-A LMF and TRUMPF Bronze 90/10-A LMF powder materials given in the batch test reports

TRUMPF 316L-A LMF		Particle distribution
Particle size distribution[a]	15–45 µm	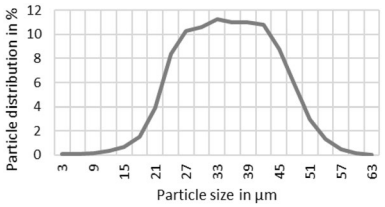
D10	22.4 µm	
D50	33.6 µm	
D90	45.1 µm	
Apparent density[b]	4.4 g/cm^3	
Flow rate[c]	14.9 s/50 g	
Chemical analysis	Cr: 16.79%; Ni: 12.76%; Mo: 2.22%; Mn: 0.68%; Si: 0.52%; Fe: Rest	
TRUMPF Bronze 90/10-A LMF		Particle distribution
Particle size distribution[a]	10–45 µm	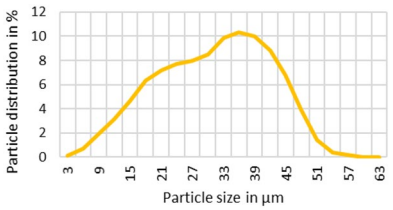
D10	13.4 µm	
D50	29.4 µm	
D90	42.6 µm	
Apparent density[b]	4.8 g/cm^3	
Flow rate[c]	15.5 s/50 g	
Chemical analysis	Sn: 10.3%; P: 0.37%; Pb: < 0.01%; Cu: Rest	

[a]Measured according ISO 13322-2, [b]Measured by Hall Flowmeter according DIN EN ISO 3923-1, [c]Measured by Hall Flowmeter according DIN EN ISO 4490

The approximated VED of specimen S1 and S2 is 109 J/mm^3 (minimum) and 290 J/mm^3. In case of specimen S3 and S4, the approximate VED is 326 J/mm^3 and 435 J/mm^3 (maximum), respectively.

The surface of the 316L specimen S1 (VED = 109 J/mm^3) shows an uneven and inhomogeneous surface topography $S1_b$ relative to the second specimen S2 (VED = 290 J/mm^3) where a rather wavy surface is visible. The reduction of the waviness is important for an alternating layered multi-material structure to reduce the mixing zones. The average height of the surface $S1_a$ changes between 500 and 550 µm at different positions with sharp fluctuations of 85 µm standard deviation $S1_b$ at measurement position three. Meanwhile, the surface of the second specimen S2 shows more even surface ($S2_a$) with less fluctuation of surface peaks. Here, the recorded standard deviation of surface height changes approximately between 55 and 60 µm ($S2_a$). Further increase of VED (326 J/mm^3 and 435 J/mm^3) demonstrates the variation of surface profile which is given in Fig. 5.

The recorded average height (at position three) of the surface of the third specimen S3 is 525 µm ($S3_a$) with standard deviation of 50 µm. In contrast, the fourth specimen S4 shows deepening towards to the center of the surface ($S4_a$). The standard deviation surface flatness of the corresponding specimen S4 changes approximately between 50 and 60 µm.

From a comparison of all four specimens S1–S4 (Figs. 4, 5), a relative low VED leads to an uneven surface with an average height between 500 and 550 µm (S1) showing sharp changes of surface peaks. Higher impose of the VED reduces the roughness to an average height between 515 and 525 µm (S2). Further increase in VED also leads to a flatter surface (S3 and S4) and minimizes the standard deviation of the surface peaks. At a maximum VED of 435 J/mm^3 (S4), an accumulation of material occurs at the edges of the exposed surface.

The cross sectional views in Fig. 6 provide a further indication on the density and the surface flatness of the corresponding 316L specimens S1-S4.

As mentioned in Figs. 4, 5, the surface topography is influenced by VED where low energy input leads to a significantly reduced density in the specimen (Fig. 6, S1). In contrast, a higher VED enables denser specimens without visible porosity (Fig. 6, S2–S4). However, the increased VED leads to a mixing zone between the substrate plate and the 316L specimens.

The detailed pictures of the marked mixing zones (a–d) in Fig. 6 are illustrated in Fig. 7.

The enlarged cross sectional view of the 316L specimens shown in Fig. 7 verifies the influence of VED on material intermixing. The diffusion zone between the substrate plate

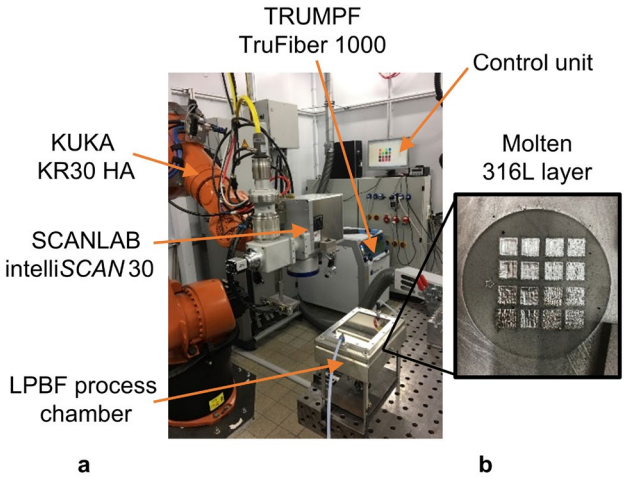

Fig. 2 **a** Experimental setup for the modular LBPF system in the laser robot cell. **b** Image of a molten layer of 316L powder

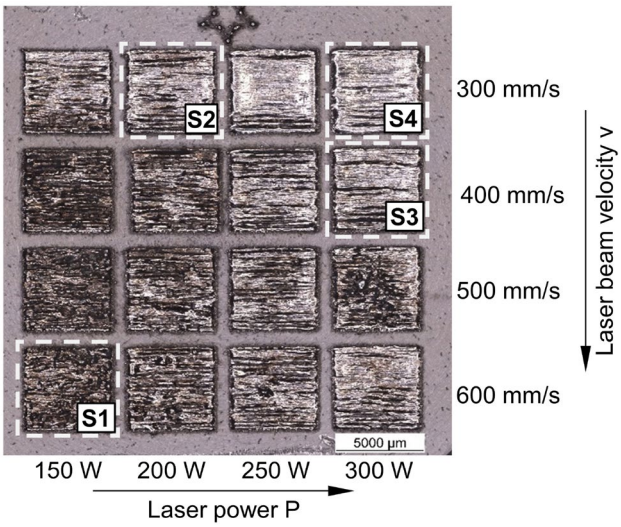

Fig. 3 Optical microscope overview image of the fabricated 316L specimens surfaces after ten layers varying laser power and laser beam velocity. The marked specimens S1–S4 are used for subsequent investigations

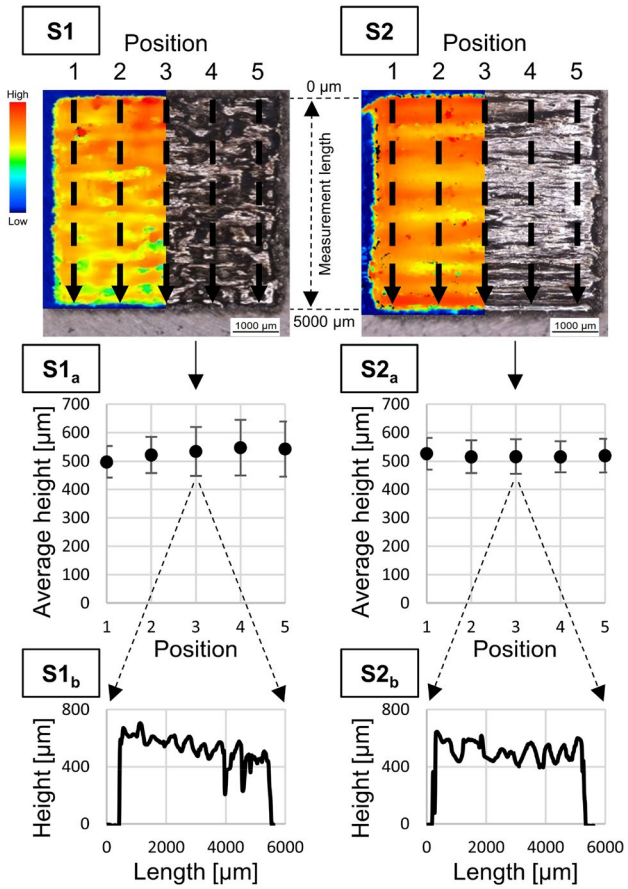

Fig. 4 **S1** Optical microscope image with associated profilometer topography of 316L specimen S1 surface after ten layers for process parameters of $P = 150$ W, $v = 600$ mm/s (VED = 109 J/mm^3). **S1$_a$** Average height of the surface at selected positions of specimen S1. **S1$_b$** Peaks of the surface at certain position marked in S1$_a$ for specimen S1. **S2** Optical microscope image with associated profilometer topography of 316L specimen S2 surface after ten layers for process parameters of $P = 200$ W, $v = 300$ mm/s (VED = 290 J/mm^3). **S2$_a$** Average height of the surface at selected positions of specimen S2. **S2$_b$** Peaks of the surface at certain position marked in S2$_a$ for specimen S2

and the 316L layers extends with an increase of VED. At a low VED, the boundary between the 316L layers and the substrate plate is clearly visible, however the specimen in Fig. 6 S1 has lack of fusion pores and a rough surface. As the VED increases, the intermixing zone increases (Fig. 7b and c), resulting in the boundary between the 316L layers and the substrate is no longer being clearly visible (Fig. 7d). However, a clear material delineation with a minimized but present mixing zone is a fundamental prerequisite for manufacturing a multi-material layered structure consisting of dissimilar materials. Otherwise, the built-up would only stick on the surface or, in case of a too high VED, an increased mixed zone with intermetallic and brittle phases would be generated.

4.2 Parameter study with Bronze

In Fig. 8, the surfaces of the final manufactured Bronze specimens during the pre-investigations after ten layers are given. In Figs. 9, 10, the surfaces of the four selected Bronze specimens B1-B4 marked in Fig. 8 are given in more detail. The approximate VED of specimen B1 and B2 is 65 J/mm^3 (minimum) and 105 J/mm^3. In case of specimen B3 and B4, the approximate VED is 146 J/mm^3 and 235 J/mm^3 (maximum).

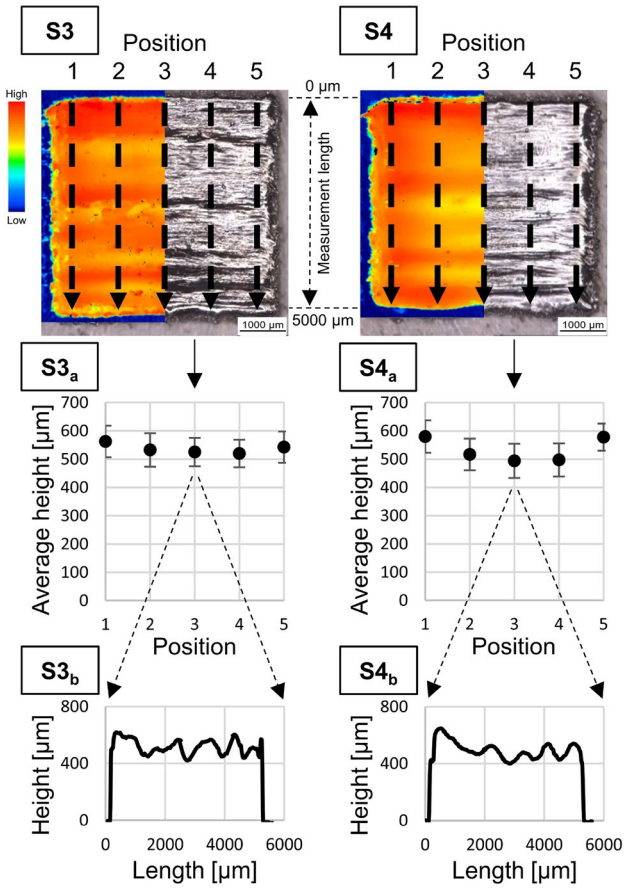

Fig. 5 **S3** Optical microscope image with associated profilometer topography of 316L specimen S3 surface after ten layers for process parameters of $P = 300$ W, $v = 400$ mm/s (VED = 326 J/mm^3). **S3$_a$** Average height of the surface at selected positions of specimen S3. **S3$_b$**) Peaks of the surface at certain position marked in S3$_a$ for specimen S3. **S4** Optical microscope image with associated profilometer topography of 316L specimen S4 surface after ten layers for process parameters of $P = 300$ W, $v = 300$ mm/s (VED = 435 J/mm^3). **S4$_a$** Average height of the surface at selected positions of specimen S4. **S4$_b$** Peaks of the surface at certain position marked in S4$_a$ for specimen S4

The surfaces of the Bronze specimens B1 (VED = 65 J/mm^3) and B2 (VED = 105 J/mm^3) show uneven melted areas (B1, B1$_b$ and B2, B2$_b$). In case of the second specimen B2, the surface seems more homogenously melted than the surface of the first specimen B1. The first specimen B1 has an average height of 380 µm (at position three B1$_a$) with a standard deviation of 38 µm. The average height of the second specimen B2 (at position three B2$_a$) is recorded 425 µm with a standard deviation of 50 µm. Further changes of VED shows a variation on the surface profile of the Bronze specimens as mentioned in Fig. 10.

The surface topography of the specimens B3 (VED = 146 J/mm^3) and B4 (VED = 235 J/mm^3) illustrates a stronger melt compared to the specimens B1 and B2. The average height of the third specimen B3 is recorded between 320 and 330 µm (B3$_a$). The minimum of the standard deviation is 30 µm, measured at position three. The fourth specimen B4 shows sharp changes in the surface flatness (B4$_a$ and B4$_b$). The resultant height at different positions changes between 350 and 380 µm and at position three, a maximum standard deviation of approximately 75 µm is recorded (B4$_a$).

Compared to 316L, the variation in VED strongly effects the height and the surface flatness of the fabricated Bronze specimens. Specimen B3 shows a smooth and even surface and the average height of the surface remains similar at different positions. At a specific energy input, a further increase in VED does not provide improved surface flatness as experienced in the case of 316L. It is observed from specimen B4 that an increase of VED imposes material accumulations at certain points which reduces the flatness of the specimen surface. At a maximum VED, the average height at different points of the specimen B4 changes up to approximately 30 µm. However, a lower VED leads to an irregular surface and porous structures which results in an increased surface height (Fig. 9). A correlation between the shiny areas of the specimen surfaces (i.e. see Fig. 8 parameter $P = 270$ W, $v = 800$ mm/s) and the surface roughness could not be found.

The cross sectional views in Fig. 11 signify the density and also the surface flatness of the corresponding Bronze specimens B1–B4.

As discussed above, the cross sectional view of the Bronze specimen B1 shows an inhomogeneous and a porous structure at low VED of 65 J/mm^3. Further increase in VED reduces the porosity and surface roughness (Fig. 11 B2 and B3). Whereby higher VED results in an increased mixing zone between the Bronze layers and the substrate plate (Fig. 11 B4).

5 Fabrication of 316L-Bronze multi-material structure

Based on the preliminary investigations of chapter 4.1 and 4.2, suitable laser power and laser beam velocity parameters for the 316L and the Bronze powder material were determined to fabricate an alternating layered multi-material structure. The selected parameters for the alternating layers are presented in Table 3. The parameters were selected regarding to the evenness of the surface, the lowest possible porosity in the built-up material and a low mixing zone with the underlying (substrate) material. As a result, e.g. the

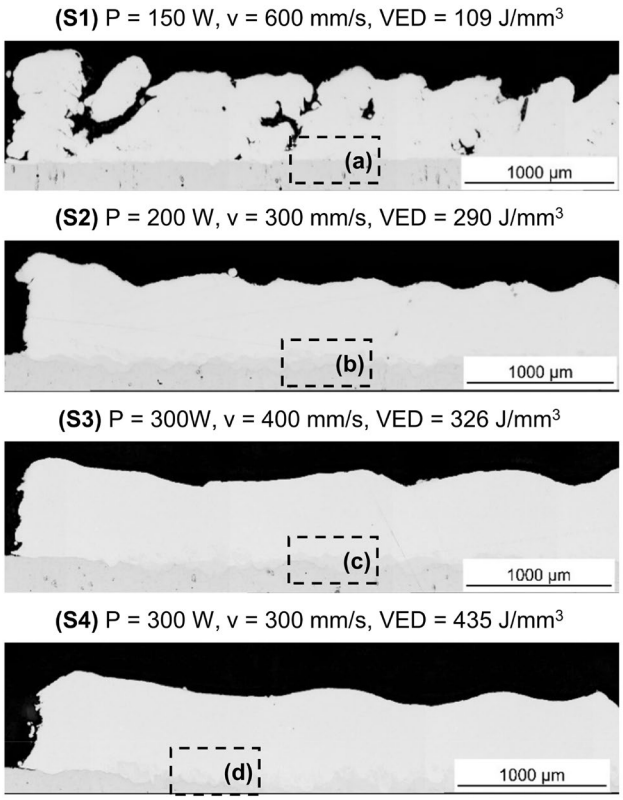

Fig. 6 Optical microscope images of cross sections of the 316L specimens S1–S4 shown in Figs. 3, 4, 5. Cross section is performed perpendicular to the hatching lines. The marked areas (**a–d**) are used for subsequent investigations

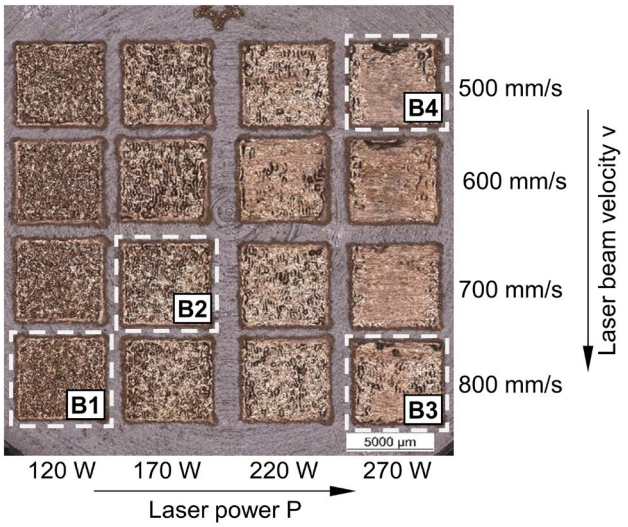

Fig. 8 Optical microscope overview image of the fabricated Bronze specimens surfaces after ten layers varying laser power and laser beam velocity. The marked specimens B1–B4 are used for subsequent investigations

Bronze parameter $P = 270$ W with $v = 800$ mm/s was used as this allows a dense build-up and causes little mixing with the underlying material (Fig. 11) although the parameter $P = 270$ W and $v = 700$ mm/s generates a more even surface (Fig. 8).

According to Table 3, initial ten layers of 316L (A) were built on the substrate plate at $P = 300$ W and $v = 400$ mm/s to achieve a fine and smooth 316L surface. For the second

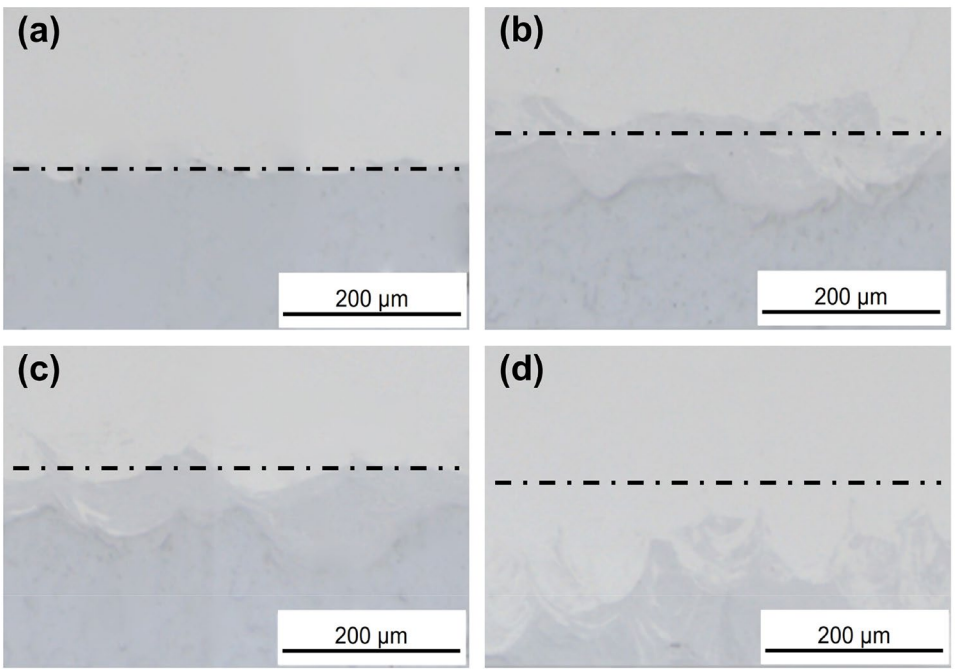

Fig. 7 Optical microscope images of higher resolution of the marked areas (**a–d**) in Fig. 6 focusing on the mixing zone between substrate plate and molten 316L layers of the cross sectional view of 316L specimens S1–S4. The dotted lines indicates the zero level of substrate plate

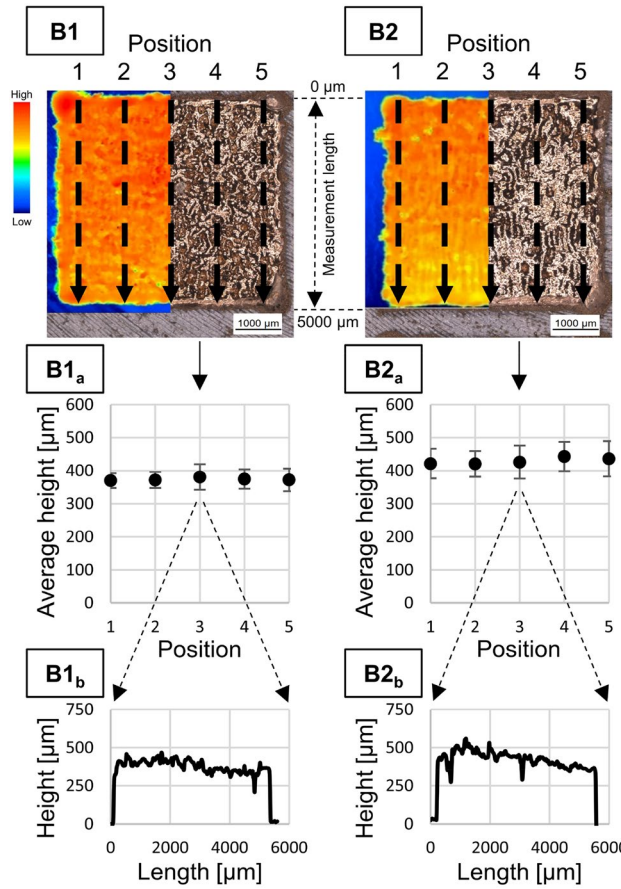

Fig. 9 **B1** Optical microscope image with associated profilometer topography of Bronze specimen B1 surface after ten layers for process parameters of $P = 120$ W, $v = 800$ mm/s (VED = 65 J/mm^3). **B1$_a$** Average height of the surface at selected positions of specimen B1. **B1$_b$** Peaks of the surface at certain position marked in B1$_a$ for specimen B1. **B2** Optical microscope image with associated profilometer topography of Bronze specimen B2 surface after ten layers for process parameters of $P = 170$ W, $v = 700$ mm/s (VED = 105 J/mm^3). **B2$_a$** Average height of the surface at selected positions of specimen B2. **B2$_b$** Peaks of the surface at certain position marked in B2$_a$ for specimen B2

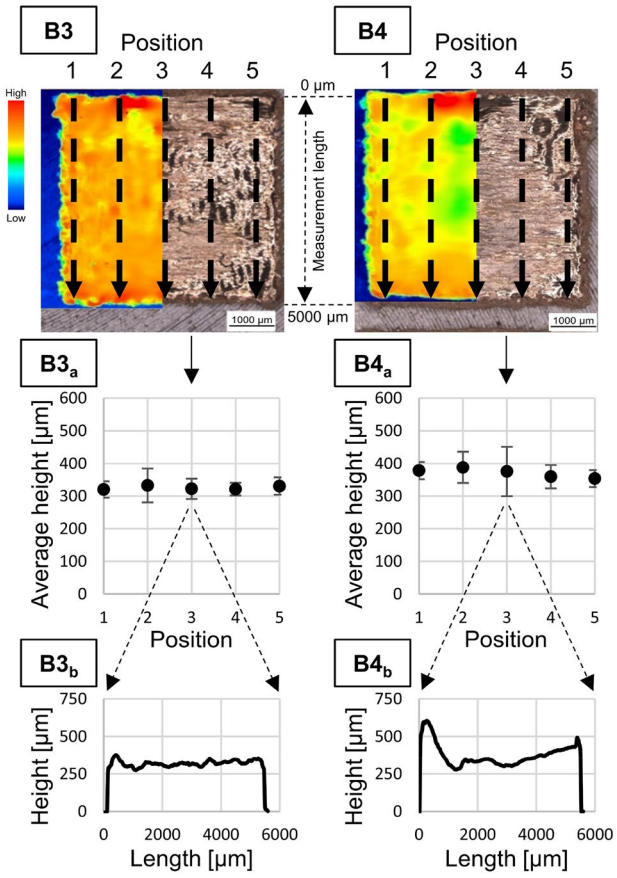

Fig. 10 **B3** Optical microscope image with associated profilometer topography of Bronze specimen B3 surface after ten layers for process parameters of $P = 270$ W, $v = 800$ mm/s (VED = 146 J/mm^3). **B3$_a$** Average height of the surface at selected positions of specimen B3. **B3$_b$** Peaks of the surface at certain position marked in B3$_a$ for specimen B3. **B4** Optical microscope image with associated profilometer topography of Bronze specimen B4 surface after 10 layers for process parameters of $P = 270$ W, $v = 500$ mm/s (VED = 235 J/mm^3). **B4$_a$** Average height of the surface at selected positions of specimen B4. **B4$_b$** Peaks of the surface at certain position marked in B4$_a$ for specimen B4

ten layers of 316L (B), $P = 250$ W and $v = 400$ mm/s was selected to avoid a mixing zone between the 316L and the Bronze layer at the interface area and to reduce the energy input into the specimen. In case of the Bronze layers, the process parameters were fixed for both layers A and B at $P = 270$ W and $v = 800$ mm/s to five layers each.

In Fig. 12, the cross section of the layered 316L-Bronze multi-material structure is given.

The cross sectional view of the layered 316L-Bronze multi-material structure shows that both types of material layers have a relatively low porosity. The interfacial boundaries of the different material layers are clearly visible and mixing between the materials is minimal due to the adapted laser parameters. The dashed section marked area in Fig. 12 is given in a more detailed image (Fig. 13).

From Fig. 13, the bottom interaction zone (a) between the 316L and the Bronze is even and the amount of the intermixing areas are minimized. In the second transition zone (b), both materials are mixed within approximately 50 µm. In this 316L layer, micro cracks in the vertical direction are visible. The reason for the appearance only on the Bronze to 316L side may be attributed to following arguments: Bronze has a melting point range of approx. 762–930 °C where the 316L has approx. 1371–1399 °C [13]. If the VED is just enough to melt up the Bronze slightly over its melting point,

the 316L is not in the molten state. Vice versa, the temperature of the molten 316L leads to a melting process of the Bronze. Due to the mixing of both materials, intermetallic phases occur. Liu et al. observed cracks at the intermetallic mixing zone in a layered structure of 316L/C18400 (copper alloy) [35]. Several investigations addressed the formation of the cracks due to the physical property mismatch (thermal expansion, heat conduction, etc.) and the infiltration of the copper into the austenitic grain boundaries in steel. Comparable vertical cracks in the boundary of the 316L layer as in Fig. 13 were found in the work of Chen et al. and Bai et al. where the cracks were attributed to the thermal expansions of the used copper alloys which are higher than the 316L [36, 37]. In addition, dendritic cracks which went perpendicular to the boundary of the interface were generated by the higher thermal conductivity of the Cu10Sn which concentrate the heat in the interface and cause thermal stress [36]. In investigation on laser metal deposition, it was recognized by Makarenko et al. that the different coefficients of thermal expansion lead to stresses in deformations in the transition zone at the grain boundaries of the intermetallic phase [38]. Further cooling result in cracks that run vertically into the material [39], which also occur in our investigations, Fig. 13.

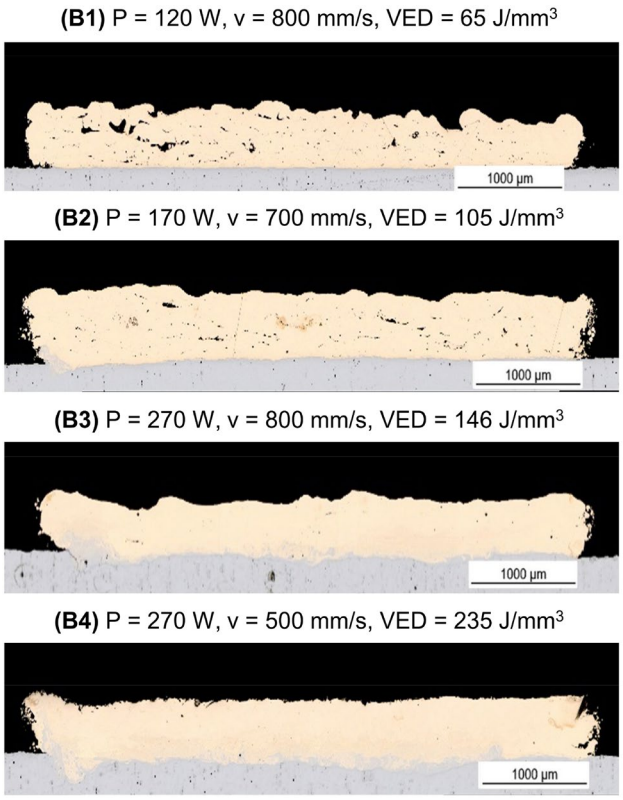

Fig. 11 Optical microscope images of cross sections of the Bronze specimens B1–B4 shown in Figs. 8, 9, 10. Cross section is performed perpendicular to the hatching lines

Table 3 Laser parameters and the number of layers for 316L and Bronze for building the alternating layered structure

Parameters for alternating layered structure			
Material	Laser power (W)	Laser beam velocity (mm/s)	Number of layers
316L (A)	300	400	10
316L (B)	250	400	10
Bronze (A)	270	800	5
Bronze (B)	270	800	5

To avoid these crack formations, the following methods have been successfully demonstrated or proposed in the literature: (I) increasing the heat input to reduce stress by adjusting the laser and build-up process [38], optimized process parameter [40] or using a process chamber heating, and (II) interlayer with a compatible material [39]. An improvement should be also achieved by (III) reducing the mixed material zone and an even transition zone. The minimized roughness and thus mixing zone may lead to reduced brittle phases, minimized liquid metal embrittlement. However, this theory still needs to be proven in further studies.

6 Conclusions

The presented novel modular LPBF system allows the processing of different materials and material combinations with a small amount of powders within one additive manufacturing step. The highly flexible LPBF system is usable for different laser sources and wavelengths, processing optics and laser cells with high accessibility for process monitoring devices i.e. sensors, thermography and high speed cameras.

In this research work, an alternating layered multi-material 316L-Bronze specimen has been manufactured to demonstrate the purposes of the modular LPBF system. The parameter studies of the 316L and the Bronze specimens illustrated the influence of process parameters (especially the VED) on the surface profile, density and intermetallic mixing which helps to identify suitable parameters for building alternating layered multi-material structures. During the parameter study with 316L, it was found that a higher VED leads to a flatter surface and a higher specimen density. At the same time, a too high energy density leads to a strong mixing with the substrate plate. For Bronze it was found that increasing the VED also leads to improved specimen density and flatness. However, if the VED is too high, material accumulations built-up on the surface and the mixing zone with the substrate plate increases significantly.

The manufactured layered 316L-Bronze specimen demonstrate the feasibility of the system to produce multi-material component parts. A material mixing zone at the

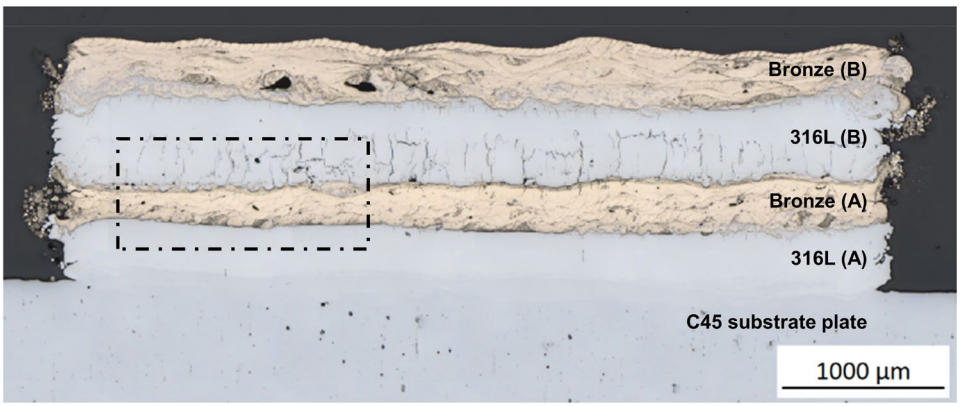

Fig. 12 Optical microscope image of the cross section of alternating layered multi-material 316L-Bronze specimen. Cross section is performed perpendicular to the hatching lines. The marked area is used for subsequent investigation

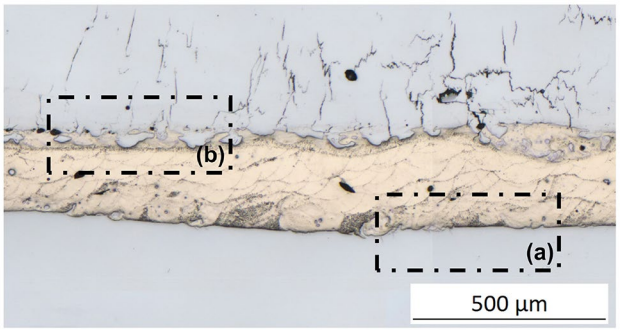

Fig. 13 Optical microscope image of higher resolution of the marked area in Fig. 12. The marked areas (**a**) and (**b**) are used for subsequent investigations

interface area and some micro cracks in the 316L layer have been investigated in the fabricated layered multi-material structure. The reason why the cracks result exclusively in the 316L layer is (I) the significantly higher melting point of 316L compared to bronze, which results in mixing when 316L is built-up on a bronze layer, (II) different thermal expansions, which causes cracks to build-up during solidification and (III) the infiltration of bronze into the grain structure of 316L. Approaches to reduce the formation of cracks were identified. These micro cracks needs attention for further investigations in this field. In addition, the future research work on modular LPBF system focusing on novel and innovative materials for LPBF.

Acknowledgements Sincere appreciation to Johannes Neuer and Steffen Mürdter, both Laser Application Center Aalen University, for their helpful support throughout the implementation of the modular LBPF system and the evaluation of the experiments.

Funding Open Access funding enabled and organized by Projekt DEAL. The authors acknowledge support by the German Federal Ministry of Education and Research within the program "FHImpuls" (Project SmartPro, Subproject Smart-ADD, Grant No. 13FH4I06IA) and "FH-Invest" (Project FlexLight 4.0, Grant No. 13FH114N6).

Declarations

Conflict of interest There is no conflict of interest associated with this publication.

Data availability The raw/processed data required to reproduce these findings cannot be shared at this time as the data also forms part of an ongoing study.

Code availability Not applicable.

References

1. Schmidt M, Merklein M, Bourell D, Dimitrov D, Hausotte T, Wegener K, Overmeyer L, Vollertsen F, Levy GN (2017) Laser based additive manufacturing in industry and academia. CIRP Ann 66:561–583. https://doi.org/10.1016/J.CIRP.2017.05.011
2. Gebhardt A (2013) Generative fertigungsverfahren: additive manufacturing und 3D drucken für prototyping—tooling—produktion. Carl Hanser Verlag, München
3. Gibson I, Rosen D, Stucker B (2015) Additive manufacturing technologies: 3D printing, rapid prototyping, and direct digital manufacturing. Springer, New York
4. Herzog D, Seyda V, Wycisk E, Emmelmann C (2016) Additive manufacturing of metals. Acta Mater 117:371–392. https://doi.org/10.1016/j.actamat.2016.07.019
5. Wei C, Li L (2021) Recent progress and scientific challenges in multi-material additive manufacturing via laser-based powder bed fusion. Virtual Phys Prototyp 16:347–371. https://doi.org/10.1080/17452759.2021.1928520
6. Tey CF, Tan X, Sing LS, Yeong WY (2020) Additive manufacturing of multiple materials by selective laser melting: Ti-alloy to

stainless steel via a Cu-alloy interlayer. Addit Manuf 31:100970. https://doi.org/10.1016/j.addma.2019.100970
7. Kruth JP, Froyen L, Van Vaerenbergh J, Mercelis P, Rombouts M, Lauwers B (2004) Selective laser melting of iron-based powder. J Mater Process Technol 149:616–622. https://doi.org/10.1016/j.jmatprotec.2003.11.051
8. Khairallah SA, Anderson AT, Rubenchik A, King WE (2016) Laser powder-bed fusion additive manufacturing: physics of complex melt flow and formation mechanisms of pores, spatter, and denudation zones. Acta Mater 108:36–45. https://doi.org/10.1016/j.actamat.2016.02.014
9. Krauss H (2017) Qualitätssicherung beim laserstrahlschmelzen durch schichtweise thermografische in-process-überwachung. Herbert Utz Verlag, München
10. Gu D (2015) Laser additive manufacturing of high-performance materials. Springer, Berlin
11. Sun S, Brandt M, Easton M (2017) Powder bed fusion processes: an overview. In: Brandt M (ed) Laser additive manufacturing: materials, design, technologies, and applications. Elsevier, Amsterdam, pp 55–77
12. Goll D, Vogelgsang D, Pflanz U, Hohs D, Grubesa T, Schurr J, Bernthaler T, Kolb D, Riegel H, Schneider G (2019) Refining the microstructure of Fe-Nd-B by selective laser melting. Phys Status Solidi RRL 13:1800536. https://doi.org/10.1002/pssr.201800536
13. Wei C, Sun Z, Chen Q, Liu Z, Li L (2019) Additive manufacturing of horizontal and 3D functionally graded 316L/Cu10Sn components via multiple material selective laser melting. J Manuf Sci Eng 141:081014. https://doi.org/10.1115/1.4043983
14. Zhang X, Wei C, Chueh YH, Li L (2019) An integrated dual ultrasonic selective powder dispensing platform for three-dimensional printing of multiple material metal/glass objects in selective laser melting. J Manuf Sci Eng 141:011003. https://doi.org/10.1115/1.4041427
15. Guo C, Ge W, Lin F (2015) Dual-material electron beam selective melting: hardware development and validation studies. Engineering 1:124–130. https://doi.org/10.15302/J-ENG-2015013
16. Wei C, Li L, Zhang X, Chueh YH (2018) 3D printing of multiple metallic materials via modified selective laser melting. CIRP Ann 67:245–248. https://doi.org/10.1016/j.cirp.2018.04.096
17. Chueh YH, Zhang X, Wei C, Sun Z, Li L (2020) Additive manufacturing of polymer-metal/ceramic functionally graded composite components via multiple material laser powder bed fusion. J Manuf Sci Eng 142:051003. https://doi.org/10.1115/1.4046594
18. Stichel T, Brachmann C, Raths M, Dechet MA, Schmidt J, Peukert W, Frick T, Roth S (2020) Electrophotographic multilayer powder pattern deposition for additive manufacturing. JOM 72:1366–1375. https://doi.org/10.1007/s11837-019-03965-z
19. Stichel T, Brandl T, Hauser T, Geißler B, Roth S (2018) Electrophotographic multi-material powder deposition for additive manufacturing. Proc CIRP 74:249–253. https://doi.org/10.1016/j.procir.2018.08.104
20. Demir AG, Previtali B (2017) Multi-material selective laser melting of Fe/Al-12Si components. Manuf Lett 11:8–11. https://doi.org/10.1016/j.mfglet.2017.01.002
21. Chivel Y (2016) New approach to multi-material processing in selective laser melting. Phys Proc 83:891–898. https://doi.org/10.1016/j.phpro.2016.08.093
22. Regenfuß P, Ebert R, Exner H (2007) Laser micro sintering—a versatile instrument for the generation of microparts. Laser Tech J 4:26–31. https://doi.org/10.1002/latj.200790139
23. Goll D, Schurr J, Trauter F, Schanz J, Bernthaler T, Riegel H, Schneider G (2020) Additive manufacturing of soft and hard magnetic materials. Proc CIRP 94:248–253. https://doi.org/10.1016/j.procir.2020.09.047
24. Wang D, Liu Y, Yongqiang Y, Xiao D (2016) Theoretical and experimental study on surface roughness of 316L stainless steel metal parts obtained through selective laser melting. Rapid Prototyp J 22:706–716. https://doi.org/10.1108/RPJ-06-2015-0078
25. Caiazzo F, Alfieri V, Casalino G (2020) On the relevance of volumetric energy density in the investigation of inconel 718 laser powder bed fusion. Materials 13:538. https://doi.org/10.3390/ma13030538
26. Tang X, Zhang S, Zhang C, Chen J, Zhang J, Liu Y (2020) Optimization of laser energy density and scanning strategy on the forming quality of 24CrNiMo low alloy steel manufactured by SLM. Mater Charact 170:110718. https://doi.org/10.1016/j.matchar.2020.110718
27. Gu D, Wang H, Dai D, Chang F, Meiners W, Hagedorn YC, Wissenbach K, Kelbassa I, Poprawe R (2015) Densification behavior, microstructure evolution, and wear property of TiC nanoparticle reinforced AlSi10Mg bulk-form nanocomposites prepared by selective laser melting. J Laser Appl 27:S17003. https://doi.org/10.2351/1.4870877
28. Vilanova M, Escribano-García R, Guraya T, San Sebastian M (2020) Optimizing laser powder bed fusion parameters for IN-738LC by response surface method. Materials 13:4879. https://doi.org/10.3390/ma13214879
29. Yasa E, Kruth J (2011) Application of laser re-melting on selective laser melting parts. Adv Prod Eng 6:259–270
30. Metelkova J, Vanmunster L, Haitjema H, Ordnung D, Kruth JP, Van Hooreweder B (2021) Hybrid dual laser processing for improved quality of inclined up-facing surfaces in laser powder bed fusion of metals. J Mater Process Technol 298:117263. https://doi.org/10.1016/j.jmatprotec.2021.117263
31. Horn M, Prestel L, Schmitt M, Binder M, Schlick G, Seidel C, Reinhart G (2020) Multi-material additive manufacturing—recycling of binary metal powder mixtures by screening. Proc CIRP 93:50–55. https://doi.org/10.1016/j.procir.2020.04.098
32. Svoboda J (2004) Magnetic techniques for the treatment of materials. Kluwer Academic Publishers, Dordrecht
33. Simmons JC, Chen X, Azizi A, Daeumer MA, Zavalij PY, Zhou G, Schiffres SN (2020) Influence of processing and microstructure on the local and bulk thermal conductivity of selective laser melted 316L stainless steel. Addit Manuf 32:100996. https://doi.org/10.1016/j.addma.2019.100996
34. Zeng C, Zhang B, Hemmasian Ettefagh A, Wen H, Yao H, Meng WJ, Guo S (2020) Mechanical, thermal, and corrosion properties of Cu-10Sn alloy prepared by laser-powder-bed-fusion additive manufacturing. Addit Manuf 35:101411. https://doi.org/10.1016/j.addma.2020.101411
35. Liu ZH, Zhang DQ, Sing SL, Chua CK, Loh LE (2014) Interfacial characterization of SLM parts in multi-material processing: metallurgical diffusion between 316L stainless steel and C18400 copper alloy. Mater Charact 94:116–125. https://doi.org/10.1016/j.matchar.2014.05.001
36. Chen J, Yang Y, Song C, Zhang M, Wu S, Di W (2019) Interfacial microstructure and mechanical properties of 316L /CuSn10 multi-material bimetallic structure fabricated by selective laser melting. Mater Sci Eng A 752:75–85. https://doi.org/10.1016/j.msea.2019.02.097
37. Bai Y, Zhang J, Zhao C, Li C, Wang H (2020) Dual interfacial characterization and property in multi-material selective laser melting of 316L stainless steel and C52400 copper alloy. Mater Charact 167:110489. https://doi.org/10.1016/j.matchar.2020.110489
38. Makarenko K, Dubinin O, Shornikov P, Shishkovsky I (2020) Specific aspects of the transitional layer forming in the aluminium bronze—stainless steel functionally graded structures after laser metal deposition. Proc CIRP 94:346–351
39. Dharmendra C, Shakerin S, Janaki Ram GD, Mohammadi M (2020) Wire-arc additive manufacturing of nickel aluminum bronze/stainless steel hybrid parts—Interfacial characterization,

prospects, and problems. Materialia 13:100834. https://doi.org/10.1016/j.mtla.2020.100834
40. Chen K, Wang C, Hong Q, Wen S, Zhou Y, Yan C, Shi Y (2020) Selective laser melting 316L/CuSn10 multi-materials: Processing optimization, interfacial characterization and mechanical property. J Mater Process Technol 283:116701. https://doi.org/10.1016/j.jmatprotec.2020.116701